Journal of Electron Spectroscopy and Related Phenomena 276 (2024) 147477

Contents lists available at ScienceDirect

Journal of Electron Spectroscopy and Related Phenomena

journal homepage: www.elsevier.com/locate/elspec

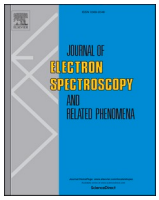

Synchrotron scanning transmission x-ray spectro-microscopy (STXM) characterisation of β-SiC nanowhisker AZ91 magnesium alloy nanocomposites

Zhuocheng Xu [a], Xinyi Hao [a], Yuting Dai [b,c], Christian Kübel [b,c,d], Milo S.P. Shaffer [e,f], Benjamin Watts [g], Qianqian Li [a,*]

[a] Department of Aeronautics, Imperial College London, London SW7 2AZ, United Kingdom
[b] Institute of Nanotechnology, Karlsruhe Institute of Technology, Hermann-von-Helmholtz-Platz 1, Eggenstein-Leopoldshafen 76344, Germany
[c] Department of Materials and Earth Sciences, Technical University of Darmstadt (TUD), Darmstadt 64287, Germany
[d] Karlsruhe Nano Micro Facility, Karlsruhe Institute of Technology, Hermann-von-Helmholtz-Platz 1, Eggenstein-Leopoldshafen 76344, Germany
[e] Department of Materials, Imperial College London, South Kensington Campus, London SW7 2AZ, United Kingdom
[f] Department of Chemistry, Molecular Sciences Research Hub (MSRH), Imperial College London, 82 Wood Lane, London W12 0BZ, United Kingdom
[g] Paul Scherrer Institute, Villigen-PSI, 5232, Switzerland

ARTICLE INFO

Keywords:
Mg alloy nanocomposites
SiC nanowhiskers
Synchrotron scanning transmission x-ray spectro-microscopy (STXM)
Interfacial phases
X-ray absorption spectrum (XAS) data analysis
Phases identification

ABSTRACT

β-SiC nanoparticles are one of the most common reinforcements in Mg-Al alloy matrix nanocomposites (MgMNCs). The interfacial interactions between β-SiC and the alloy matrix are complex due to the occurrence of new phases and the fine scale of the 3D architecture. This study aims to explore the feasibility of using synchrotron Scanning Transmission X-ray spectro-Microscopy (STXM) to investigate such interfacial interactions and acquire reference X-ray Absorption Spectroscopy (XAS) data for some common interphase crystals present within the composites, which are not readily available. Throughout this study, a reliable procedure for collecting STXM data on samples derived from MgMNCs was developed, and reference XAS spectra for α-Mg, β-$Mg_{17}Al_{12}$, T2-Al_2MgC_2, Mg_2Si and MgO present in MgMNCs were collected. The accessibility of STXM and spatially resolved XAS spectrum is not only useful for nanocomposite alloy research but applicable widely across the magnesium alloy research community when identifying and quantifying the phases with complex crystal structures and oxide states.

1. Introduction

Mg matrix nanocomposites (MgMNCs) are promising lightweight structural materials for the automotive and aeronautics industries given their high strength at intrinsically low densities [1,2]. Among these nanocomposites, AZ series alloy matrices (Mg alloyed with Al and Zn) reinforced by SiC nanoparticles (NPs) are some of the most frequently researched [3,4], motivated by wide material availability, excellent mechanical performance and good wettability during the melt manufacturing process [3,4].

This good interfacial compatibility between SiC and Mg-Al alloys has been attributed to the good lattice match between β-SiC and α-Mg phase [5–8] as well as specific interfacial reactions between β-SiC and Mg-Al alloy melt [9–11]. During the interfacial reactions, a variety of binary or ternary carbides containing Mg and Al may occur; some typical examples include Al_4C_3 [12], MgC [13], AlC_2 [14] and Al_2MgC_2 [15–17]. Despite numerous studies detailing the compositions and crystallographic information of these carbides, their formation mechanisms and orientations relationships with the α-Mg phase have not been fully characterised [18–21]. This lack of comprehensive understanding is likely attributed to the challenges associated with sample preparation, particularly due to the easily hydrolysable nature of these carbides [17]. A deeper comprehension of these interphase crystals sheds light on their impact on the microstructure of MgMNCs. This includes effects such as nanofiller dispersion and associated grain refinement, along with the corrosion resistance of the composites, which collectively define the performance of the composite materials.

Scanning transmission X-ray spectro-microscopy (STXM) at PSI,

* Corresponding author.
E-mail address: qianqian.li@imperial.ac.uk (Q. Li).

https://doi.org/10.1016/j.elspec.2024.147477
Received 30 May 2024; Received in revised form 24 August 2024; Accepted 27 August 2024
Available online 30 August 2024

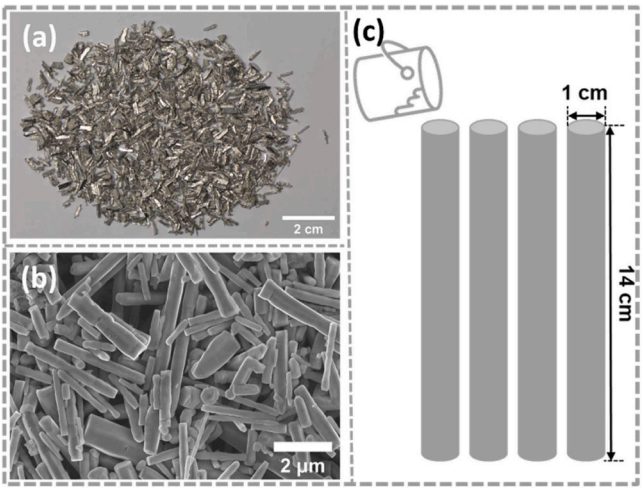

Fig. 1. (a) Image of the AZ91D machinery chips used in our study. (b) SEM image of the as-received β-SiC_{nw} used in this study. (c) Sketch of the ingots obtained after gravity casting.

Switzerland, provides new opportunities to characterise these interphase crystals within a sample with micron-scale thickness. STXM provides direct transmission images of the sample microstructure (with spatial resolution around tens of nanometres [22,23]) together with a spatially resolved X-ray absorption spectroscopy (XAS) spectrum (with energy resolution around 0.5 eV) [24–26]; the resulting spectral imaging provides both morphology and some crystallographic information, in principle allowing the atomic coordinates, electronic structure and crystal symmetry of the interfacial products to be determined. To analyse the XAS spectrum of an unknown phase, the most common approach is to compare its spectral feature with a library of reference compounds. However, to our knowledge, the spectra of some common phases in the β-SiC reinforced Mg-Al matrix nanocomposite are not readily available in literature. Hence, in this work, we aimed to capture reference XAS spectra on phases identified at β-SiC nanowhiskers (SiC_{nw}) – AZ91 interface, confirmed by high resolution electron microscopy.

2. Experimental

The β-SiC_{nw} reinforced AZ91 matrix nanocomposite was manufactured by melt stirring and gravity casting as in our previous publication [2]. 140 g of AZ91D machinery chips (Fig. 1(a) and the detailed elemental composition in Table 1, provided by non ferrum GmbH, Austria) were first melted in a boron nitride coated steel crucible at 650 °C under Ar gas protection. After ensuring the chips were melted completely, 1 vol% β-SiC_{nw} powder was then added to the melt, wrapped in an Al foil packet. The β-SiC_{nw} used in this study was provided by Haydale Ltd (USA) with average diameter and length of 0.44 ± 0.10 µm and 5.48 ± 0.17 µm, respectively (confirmed with multiple SEM images; example shown in Fig. 1(b)). The mixture was subsequently stirred at 390 RPM for 2 hours before casting into a steel mould pre-heated at 200 °C. In the last 5 min of stirring, the melt temperature was increased to 680 °C to improve fluidity during casting. The cast ingot consisted of four cylindrical rods with each rod of 1 cm in diameter and 14 cm in height (Fig. 1(c)). For comparison, reference samples made from pure AZ91 alloy were also prepared following the same casting process. Finally, to obtain the XAS spectrum of MgO formed during the stir-casting process, a pure AZ91 sample was also prepared without adequate Ar protection during stir-casting at 650°C.

To analyse the interphase crystals between SiC_{nw} and AZ91 matrix, cross-sections from different parts of the casted ingots were cut, ground and polished based on the standard metallographic sample preparation steps for AZ91 alloys [18]. To avoid oxidation of Mg matrix and hydrolysis of any carbide phases, water was strictly avoided during the grinding and polishing process. Before Scanning electron microscopy (SEM), all the cross-sections were subjected to Ar ion polishing at 4 kV voltage and 1° gun tilt for 8 hours to eliminate any hydrolysed carbides and oxides formed during sample transportation and protruding SiC_{nw} on the cross-sections (formed during grinding and polishing due to the soft Mg alloy matrix).

The microstructural analysis was conducted using a Zeiss Sigma-300 SEM (Zeiss, Germany). Initially, the phase distributions were examined in backscattered (BSD) electron mode, utilising an acceleration voltage of 20 keV and working distance of 15 mm. Subsequently, the phases of interests were further investigated in secondary (SE) electron mode with an acceleration voltage of 5 keV and working distance of 5 mm.

To further identify the phases of interest within MgMNC and establish reference areas for XAS spectra analysis, energy dispersive X-ray (EDX) spectroscopy (Bruker, Germany) was performed using SE-SE setup. For the carbide phases formed at SiC_{nw} – AZ91 interface, Electron Backscatter Diffraction (EBSD) and Scanning Transmission Electron Microscopy (STEM) were employed to analyse their crystal structure, interfaces, and local chemistry.

In this study, the EBSD analysis was performed using Bruker eFlash detector (Bruker, Germany) equipped in Zeiss Sigma-300 SEM with the SEM-BSD setup and 70° sample tilt. STEM examination was carried out using the High-Angle Annular Dark Field (HAADF) detector equipped in the Themis-Z double corrected analytical STEM (ThermoFisher, USA), operating at 300 keV. The sample for STEM was prepared using strata (ThermoFisher, USA) Focus Ion Beam (FIB), following the standard lift-out procedure for TEM sample preparation.

The STXM measurement was carried out in the Pollux beamline at PSI [25,26]. During the measurement, a 25 nm zone plate was used to focus the monochromatised soft X-ray beam onto a sample and the transmitted beam intensity was recorded as a function of sample position and photon energy in order to produce X-ray images or XAS spectra. The lamella samples for STXM were prepared by FIB Helios (ThermoFisher, USA) with standard lift-out procedure for TEM sample except that the lamella for STXM were thicker. The samples were kept at 12 µm in width and 5 µm in height so that the phases of interest, as pre-determined by SEM, were included. The thickness of the lamella was determined by the thickness of the phases of interest, therefore it was kept less than 2.5 µm to avoid overlapped spectra (caused by other phases near the interface) and match the soft X-ray attenuation length in Mg [24]. Besides, the potential influence of ion beam damage during FIB and X-ray radiation damages during STXM scanning on XAS spectrum was believed to be negligible considering much larger sample thickness in comparison to the ion beam damage layer [27] and good phases stabilities within Mg-Al alloys under ionising radiation [28].

During STXM scanning, regions of interest (ROIs) were first identified by single-energy images across the whole lamella area. Then, the ROIs were subsequently examined by X-ray spectral maps across the energy ranges of the Mg and Al K-edges. Table S1 in the supplementary document summarised the specific STXM experimental parameters used in this study including scanned energy range, scanning step size and energy step size. These values were determined based on the energy

Table 1
Elemental composition of AZ91 alloys in weight percent provided by non-ferrum GmbH.

Mg	*Al*	*Zn*	*Mn*	*Si*	*Cu*	*Ni*	*Fe*	*Be*	*others*
Balance	*8.500–9.500*	*0.450–0.900*	*0.170 – 0.400*	*0.000 – 0.080*	*0.000 – 0.025*	*0.000 – 0.001*	*0.000 – 0.004*	*0.000 – 0.001*	*0.000 – 0.010*

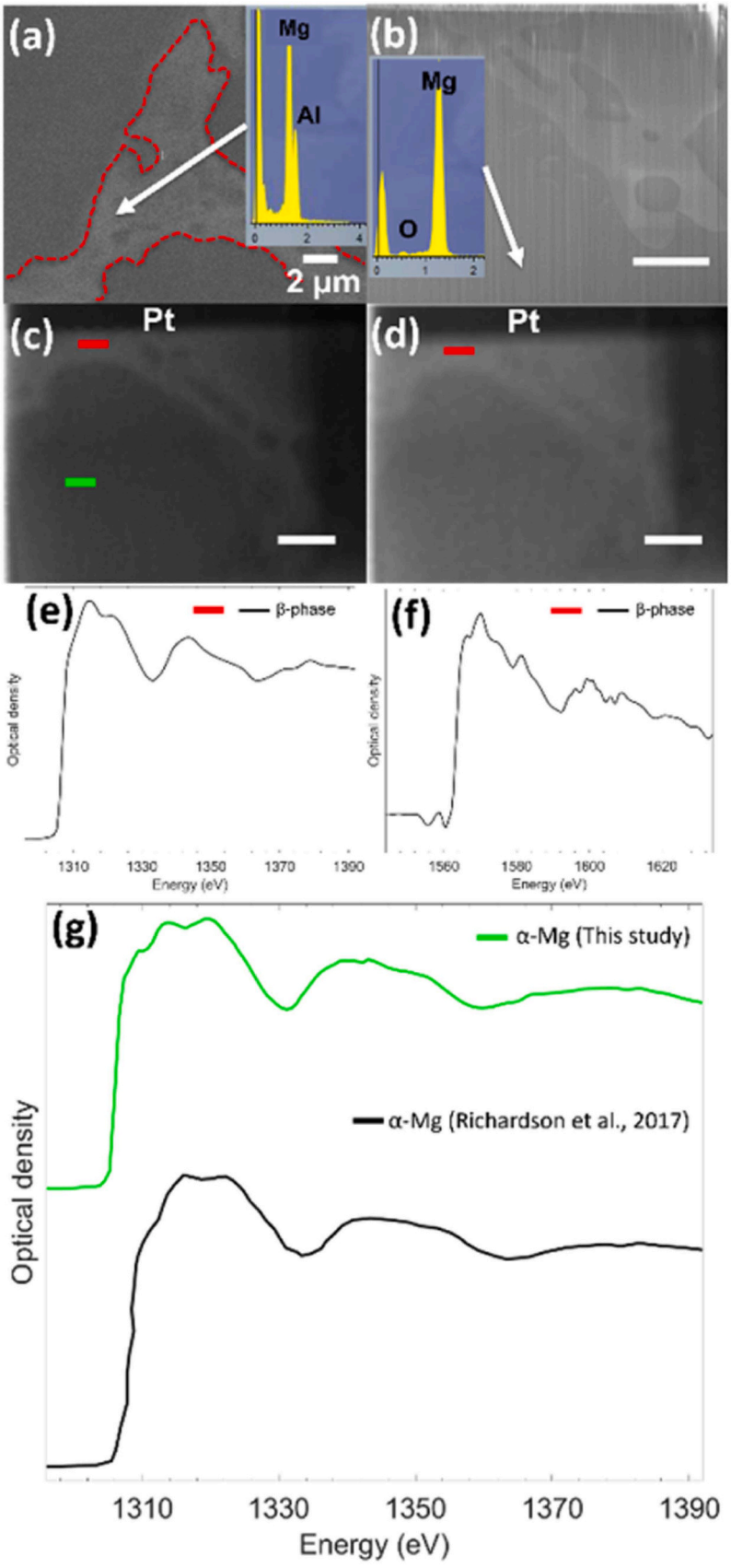

(caption on next page)

Fig. 2. (a) SEM-secondary electron (SEM-SE) image of the sample used for capturing reference XAS spectrum for β-phase (outlined by red dotted line) and α-Mg (remainder). (b) SEM-SE image of the cross-section before lifting out during FIB preparation. The insets of these two images are the collected by EDX point analysis. (c) STXM image captured near Mg K-edge at 1315 eV. (d) STXM image captured near Al K-edge at 1587 eV. The scalebars in images (a), (b), (c) and (d) are 2 μm. The red line in panel (c) and (d) and the green line in (c) indicate the position of the line scan used for capturing XAS of β-phase and α-Mg phase. (e) The XAS spectrum for β-phase near Mg K-edge. (f) The XAS spectrum for β-phase near Al K-edge. (g) The XAS spectrum for α-Mg near Mg K-edge captured in this study (green line) and replotted from Richardson et al. [37] (black line).

range of Mg and Al K-edge and theoretical energy (around 1.5 eV) and spatial resolution (around 100 nm) of the STXM at PolLux beamline. Depending on the dimensions of ROIs and the necessity of acquiring its STXM images, the scanning mode can be either along a line ('line scan' for features with a relatively large dimension and/or when microstructural information is not necessary) or across a 2D section ('stack scan' for features with a relatively small dimension and/or when microstructural information is important).

Following STXM scanning, aXis2000 software [29] was used to process the XAS spectra and images acquired during the experiment. During the XAS spectrum extraction, the optical density (OD) of the spectra was obtained by normalising the transmitted X-ray intensity with respect to the incidence intensity (measured via an empty sample region). The energies of all the XAS spectra were calibrated by using standard MgO spectrum [30–32]. Further analysis such as image stacking, spectra comparison and linear combination fitting were performed in ImageJ, MATLAB 2023 and Larch software [33], respectively.

3. Results and discussion

In order to capture the XAS spectra of the β-phase, α-Mg, T2-Al_2MgC_2 carbide, Mg_2Si and MgO phases, SEM and EDX point analysis were first carried out to locate suitable regions for the STXM sample, and to confirm the local composition (Figs. 2–5). For the carbide phase identified at β-SiC_{nw} – AZ91 interface, additional EBSD and TEM analysis were carried out to confirm their crystal structures (Fig. 3(c) to (f)) due to the possibility of forming different polymorph. Based on the indexed Selected Area Electron Diffraction (SAED) pattern showed in Fig. 3(f), the carbide phase formed was identified as T2-Al_2MgC_2 with the calculated lattice parameters of a = 3.4075 $\dot{A}$ and c = 5.8120 $\dot{A}$. These values were closed to the theoretical lattice parameters of this crystal determined by X-ray powder diffraction with a = 3.3770 $\dot{A}$ and c = 5.8171 $\dot{A}$ [34,35].

To avoid the possible influence of the SiC_{nw} addition, the lamellae containing β-phase and α-Mg were selected from the polished cross-section obtained from the pure AZ91 sample (Fig. 2(a) & (b)). During the STXM experiment, 'line scans' at the positions indicated in Fig. 2(c) & (d) were carried out to acquire the XAS spectra of these two phases. For samples containing MgO, Mg_2Si and T2-Al_2MgC_2 phases, 'stack scans' were carried out to capture their STXM images at different energy steps and compensate the influence of sample drifting. In the post-analysis of the 'stack scan', the scanning data was initially aligned based on the STXM images at different energy steps. Subsequently, regions of interest (corresponding to the positions of the phases) for generating XAS spectra were determined from the STXM images (Fig. 3(g) & (h), Fig. 4(c) and Fig. 5(c)) based on the contrast formed via X-ray absorption and by aligning with the SEM image of the lamella sample collected after FIB cutting.

The XAS spectra of all the phases collected in this study were plotted together in Fig. 6(a) & (b). By considering the energy shift related to the rising edge, regions within these spectra can be categorised as X-ray absorption near-edge structure (XANES) or extended X-ray absorption fine structure (EXAFS) [36]. In this study, we designated the region before first destructive interference observed (around 1333 eV in Mg K-edge and around 1592 eV in Al K-edge) within the spectrum as XANES and the region afterwards as EXAFS. Tables 2 and 3 summarised the energy positions of some features observed at XANES of the phases collected in this study. After comparing the relative energy positions of these features, with respect to the rising edge, similar energy positions were noted for the features identified between α-Mg and β-phase as well as between MgO and Mg_2Si. This observation could be attributed to the similar Mg oxide states within these two pairs of phases. Additionally, by comparing the features at EXAFS, the spectrum of MgO exhibited distinct constructive and destructive energy positions compared to the spectra of the other phases (Fig. 6(a)). By considering the formation mechanism of MgO during Mg melt oxidation, this difference might be explained the small particle size (100 nm) and powder nature of the MgO [37].

To confirm the reliability of the measurements, where available, reference XAS spectrum available from previous research were replotted for comparison. From the comparison for the XAS spectrum for α-Mg (Fig. 2(g)) [38] and MgO (Fig. 5(d)) [24,30], similar spectral shapes and relative peak positions (Table 2) were identified which confirms the reliability of the current procedures to capture reference NEXAFS spectrum.

To illustrate the applicability of these reference spectra in STXM analysis, the new XAS spectra were used to probe additional unidentified phases within the lamella presented in Fig. 3. The locations of these phases were identified based on their contrast in STXM images captured near the Mg K-edge and Al K-edge (Fig. 7(a&b)), which was due to their varying X-ray absorption. By direct comparisons and linear combination fittings of these extracted XAS spectra with the reference spectra presented in Fig. 6 (Figure S1 and Table S2), the predominantly interphase crystals at ROI 1–3 were identified as: T2-Al_2MgC_2, α-Mg, and a combination of T2-Al_2MgC_2 and α-Mg, respectively. This result highlights the utility of the reference spectra collected in this work for compositional analysis after STXM spectral imaging. Coupling the compositional information with the morphological details provided by STXM images can provide insights into interphase crystals, both their 3D morphologies [23] and their interaction with other constituents. Such information is challenging to acquire using other characterisation techniques with comparable resolution and sample dimensions.

4. Conclusion

In this work, X-ray absorption spectroscopy (XAS) spectra for several common phases identified near the β-SiC_{nw} - AZ91 interface were collected using synchrotron STXM at the energy range near Mg and/or Al K-edge for the first time. To prepare the sample for STXM analysis, analytical SEM and TEM were first used to identify the phases of interest. The common FIB lift-out procedure was then followed to obtain the lamellae for the STXM scans. Comparisons of the NEXAFS spectra obtained for α-Mg and MgO with the spectra reported from the literature, confirmed the validity of the sample preparation and data reduction approaches. This observation increased our confidence for the accuracy of XAS spectra for other phases captured in this study.

The results of this study provided a basis for using STXM as a technique to probe the sub-micron scale features near reinforcements-matrix interface β-SiC reinforced AZ91 matrix, especially the phases with polymorphs of different crystal structures and element oxidation states. The ternary carbides [18] highlighted in this work, along with the AlMn intermetallic phases studied previously [39], play an important role in the development of these alloy nanocomposites. In future work, efforts will focus on expanding the XAS spectra databases for other important interfacial phases such as AlMn intermetallics [39] and various carbides [18], at different element edges (e.g. Si K-edge and Mn L-edge).

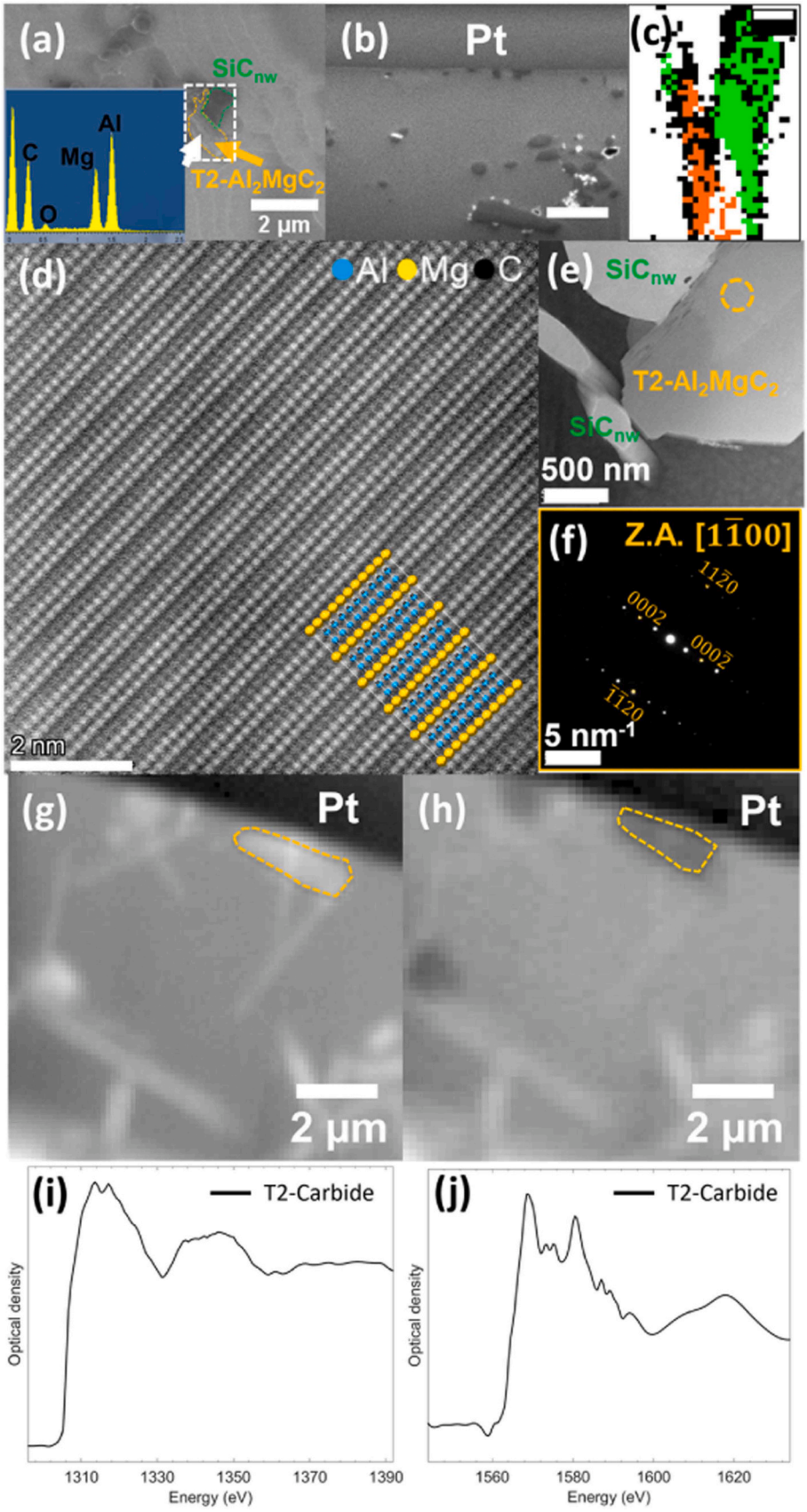

(caption on next page)

Fig. 3. (a) SEM-secondary electron (SEM-SE) image of the sample used for capturing reference XAS spectrum for T2-Al_2MgC_2 phase. The inset is the spectrum collected by EDX points analysis. (b) SEM-SE image of the cross-section before lifting out during FIB preparation. The scalebar in this image is 2 μm. (c) EBSD phase mapping of the T2-Al_2MgC_2 used for capturing reference spectrum, in which the orange colour indicates T2-Al_2MgC_2 phase, the green colour indicates β-SiC_{nw} and white colour indicates α-Mg phase. The black colour indicates non-indexed pixels. The scalebar in this image is 500 nm. The region for this EBSD was labelled with white box in (a). (d) Atomic resolution STEM image of T2-Al_2MgC_2 phase captured at [$1\bar{1}00$] zone axis. The lattice of T2-Al_2MgC_2 was superimposed on the STEM image to indicate the positions of atoms. (e) The low-magnification STEM image of the T2-Al_2MgC_2 phase. (f) The indexed electron diffraction pattern captured at the location labelled in circle in (e). (g) STXM image captured near Mg K-edge at 1315 eV. (h) STXM image captured near Al K-edge at 1587 eV. The regions outlined by yellow dotted lines in image (g) and (h) are the positions used for capturing XAS spectra. (i) The XAS spectrum for T2-Al_2MgC_2 near Mg K-edge. (j) The XAS spectrum for T2-Al_2MgC_2 near Al K-edge.

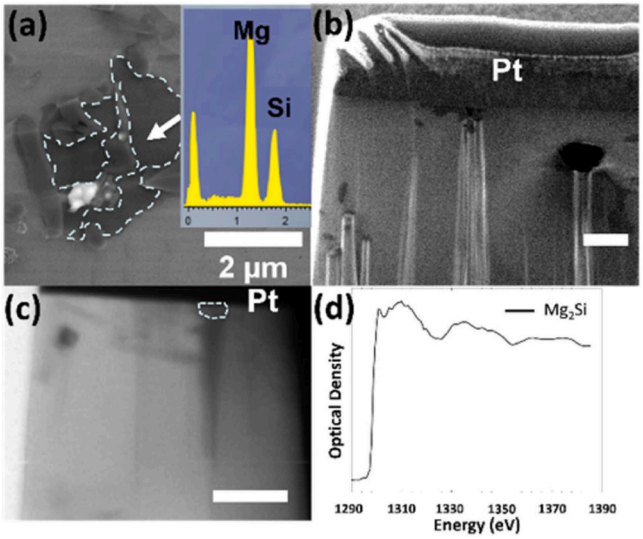

Fig. 4. (a) SEM-secondary electron (SEM-SE) image of the sample used for capturing reference XAS spectrum for Mg2Si phase (outlined by light blue colour). The inset is the spectrum collected from EDX points analysis. (b) SEM-SE image of the cross-section before lifting out during FIB preparation. (c) STXM image captured near Mg K-edge at 1315 eV. The regions outlined by light blue dotted lines in the image is the position used for capturing XAS spectrum. The scalebars in images (a), (b), and (c) are 2 μm. (d) The XAS spectrum for Mg_2Si phase near Mg K-edge.

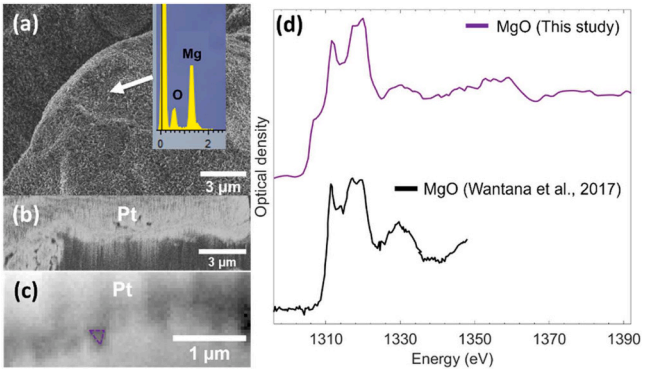

Fig. 5. (a) SEM-secondary electron (SEM-SE) image of the sample used for capturing reference XAS spectrum for MgO. The inset is the spectrum collected from EDX point analysis. (b) SEM-SE image of the cross-section before lifting out during FIB preparation. (c) STXM image captured near Mg K-edge at 1315 eV. The region outlined by purple dotted line in (c) is used for generating XAS spectrum. (d) The XAS spectrum for MgO phase near Mg K-edge captured in this study (Purple line) replotted from W. Klysubun et. al. [30] (Black line).

Additionally, simulations based on density functional theory will be considered in the future works to further improve the accuracy of the captured spectra and gain a better understanding of features in XAS spectra, especially NEXAFS [24]. Having access to these spectral data will enable us and wider research community to identify and quantify the presence of specific phase polymorphs, employing methods such as linear combination of XAS spectra.

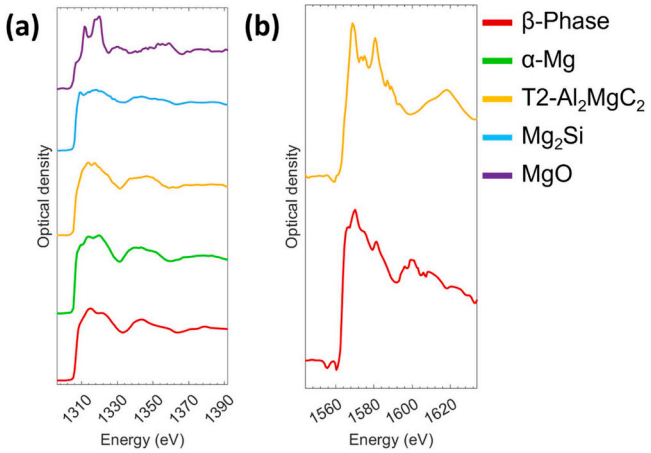

Fig. 6. XAS spectra of all the phases captured in this study at energy range (a) near Mg K-edge, and (b) near Al K-edge. The spectra of the phases were colour-coded based on the legend shown on the right hand-side.

Table 2
The near edge X-ray absorption fine structure (NEXAFS) features at Mg K-edge obtained from the XAS spectrum collected in this study.

Phase	Feature positions	Feature description	Energy shift related to Edge onset
α-Mg (This study)	1307.0	Edge onset	0.0
	1313.0	Peak	6.0
	1319.0	Peak	12.0
α-Mg (from Richardson et al. [29])	1310.0	Edge onset	0.0
	1316.3	Peak	6.3
	1321.8	Peak	11.8
β-phase	1308.0	Edge onset	0.0
	1315.0	Peak	7.0
	1321.0	Peak	13.0
Mg_2Si	1307.0	Edge onset	0.0
	1309.0	Peak	2.0
	1314.0	Peak	7.0
	1319.0	Peak	12.0
	1320.0	Peak	13.0
MgO (This study)	1310.0	Edge onset	0.0
	1312.0	Peak	2.0
	1317.0	peak	7.0
	1320.0	Peak	10.0
MgO (from Wantana et al., 2017 [30])	1310.0	Edge onset	0.0
	1311.6	Peak	1.6
	1314.1	Peak	4.1
	1317.2	Peak	7.2
	1319.7	Peak	9.7
T2-Al_2MgC_2	1307.0	Edge onset	0.0
	1314.0	Peak	7.0
	1317.0	Peak	10.0

Table 3
The near edge X-ray absorption fine structure (NEXAFS) features at Al K-edge obtained from the XAS spectrum collected in this study.

Phase	Feature positions	Feature description	Energy shift related to Edge onset
β-phase	1565.0	Edge onset	0.0
	1566.0	Peak	1.0
	1570.0	Peak	5.0
	1581.0	Peak	16.0
T2-Al_2MgC_2	1565.0	Edge onset	0.0
	1568.0	Peak	3.0
	1573.0	Peak	8.0
	1575.0	Peak	10.0
	1580.0	Peak	15.0
	1587.0	Peak	22.0
	1589.0	Peak	26.0
	1594.0	Peak	29.0

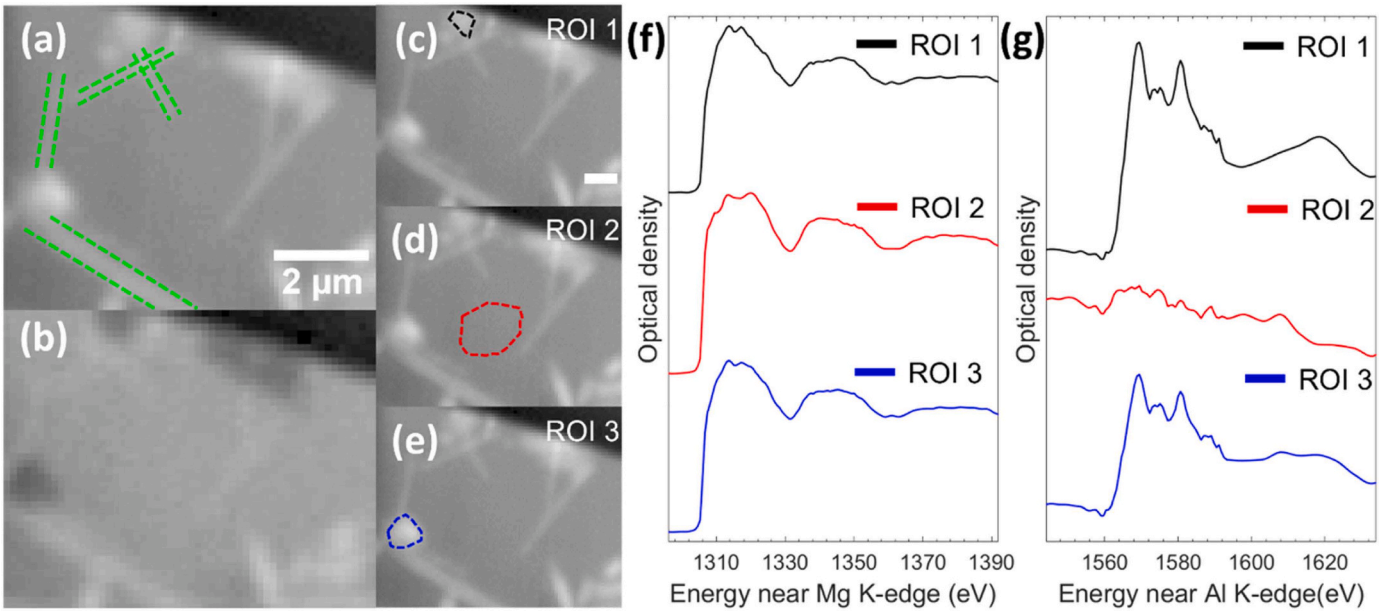

Fig. 7. STXM images of the lamella sample used for composition analysis captured at (a) 1313 eV and (b) 1588 eV, respectively. In these two images, the location of SiCnw was labelled by green dotted lines. The region of interest (ROI) 1–3 used for XAS spectrum extraction were presented in (c-e). (f) The XAS spectra of ROI 1–3 near Mg K-edge. (g) The XAS spectra of ROI 1–3 near Al K-edge. The composition analysis for these spectra can be found in Fig. S1.

CRediT authorship contribution statement

Milo S.P. Shaffer: Writing – review & editing, Supervision. **Benjamin Watts:** Writing – review & editing, Methodology, Investigation. **Yuting Dai:** Methodology, Investigation. **Christian Kübel:** Writing – review & editing, Supervision. **Qianqian Li:** Writing – review & editing, Supervision, Methodology, Investigation, Funding acquisition. **Zhuocheng Xu:** Writing – original draft, Validation, Methodology, Investigation, Formal analysis, Data curation. **Xinyi Hao:** Methodology, Investigation.

Declaration of Competing Interest

The authors declare that they have no known competing financial interests or personal relationships that could have appeared to influence the work reported in this paper.

Data availability

Data will be made available on request.

Acknowledgement

The authors wish to acknowledge PolLux beamline at the Paul Scherrer Institut (proposal 20221800) for scanning transmission X-ray microscopy. The PolLux end station was financed by the German Ministerium für Bildung und Forschung (BMBF) through contracts 05K16WED and 05K19WE2. This project has also received funding from the European Union's Horizon 2020 research and innovation programme under grant agreement No 101007417 having benefited from the access to EM facilities provided by Institution of nanotechnology, Karlsruhe Institute of Technology, Germany, within the framework of the NFFA-Europe Pilot Transnational Access Activity, proposal ID311. The help of TEM sample preparation by Miss Vanessa Wollersen is kindly acknowledged. The authors would like to acknowledge the use of characterisation facilities within the Harvey Flower Electron Microscopy Suite, Imperial College London. Finally, the authors also wish to acknowledge the technical support and great help from Mr Peter Schäffler and Mr Matthew Herbert at Non Ferrum GmbH regarding Mg AZ91 chips machining.

Appendix A. Supporting information

Supplementary data associated with this article can be found in the online version at doi:10.1016/j.elspec.2024.147477.

References

[1] Q. Li, A. Viereckl, C.A. Rottmair, R.F. Singer, Improved processing of carbon nanotube/magnesium alloy composites, Compos. Sci. Technol. 69 (2009) 1193–1199, https://doi.org/10.1016/j.compscitech.2009.02.020.

[2] Q. Li, C.A. Rottmair, R.F. Singer, CNT reinforced light metal composites produced by melt stirring and by high pressure die casting, Compos. Sci. Technol. 70 (2010) 2242–2247, https://doi.org/10.1016/j.compscitech.2010.05.024.

[3] L.-Y. Chen, J.-Q. Xu, H. Choi, M. Pozuelo, X. Ma, S. Bhowmick, J.-M. Yang, S. Mathaudhu, X.-C. Li, Processing and properties of magnesium containing a dense uniform dispersion of nanoparticles, Nature 528 (2015) 539–543, https://doi.org/10.1038/nature16445.

[4] K. Nie, K. Deng, X. Wang, K. Wu, Characterization and strengthening mechanism of SiC nanoparticles reinforced magnesium matrix composite fabricated by ultrasonic vibration assisted squeeze casting, J. Mater. Res. 32 (2017) 2609–2620, https://doi.org/10.1557/jmr.2017.202.

[5] Y.X. Chen, D.X. Li, Microstructure and orientation relationships of Mg alloy matrix composite reinforced with SiC whiskers and B4C particles, Mater. Lett. 61 (2007) 4884–4886, https://doi.org/10.1016/j.matlet.2007.03.065.

[6] K. Wu, M. Zheng, M. Zhao, C. Yao, J. Li, Interfacial reaction in squeeze cast SICW/AZ91 magnesium alloy composite, Scr. Mater. 35 (1996) 529–534, https://doi.org/10.1016/1359-6462(96)00169-8.

[7] Y. Cai, D. Taplin, M.J. Tan, W. Zhou, Nucleation phenomenon in SiC particulate reinforced magnesium composite, Scr. Mater. 41 (1999) 967–971, https://doi.org/10.1016/s1359-6462(99)00247-x.

[8] K.N. Braszczyńska, L. Lityńska, A. Zyska, W. Baliga, TEM analysis of the interfaces between the components in magnesium matrix composites reinforced with SiC particles, Mater. Chem. Phys. 81 (2003) 326–328, https://doi.org/10.1016/S0254-0584(02)00594-1.

[9] L.-X. Shi, P. Shen, D. Zhang, Q.-C. Jiang, Wetting and evaporation behaviors of molten Mg–Al alloy drops on partially oxidized α-SiC substrates, Mater. Chem. Phys. 130 (2011) 1125–1133, https://doi.org/10.1016/j.matchemphys.2011.08.051.

[10] D.S. Han, H. Jones, H.V. Atkinson, The wettability of silicon carbide by liquid aluminium: the effect of free silicon in the carbide and of magnesium, silicon and copper alloy additions to the aluminium, J. Mater. Sci. 28 (1993) 2654–2658, https://doi.org/10.1007/BF00356199.

[11] G.W. Liu, M.L. Muolo, F. Valenza, A. Passerone, Survey on wetting of SiC by molten metals, Ceram. Int. 36 (2010) 1177–1188, https://doi.org/10.1016/j.ceramint.2010.01.001.

[12] Q. An, X.-S. Cong, P. Shen, Q.-C. Jiang, Roles of alloying elements in wetting of SiC by Al, J. Alloy. Compd. 784 (2019) 1212–1220, https://doi.org/10.1016/j.jallcom.2019.01.138.

[13] A. Azad, L. Bichler, A. Elsayed, Effect of a novel Al-SiC grain refiner on the microstructure and properties of AZ91E magnesium alloy, Int. J. Met. 7 (2013) 49–58, https://doi.org/10.1007/bf03355564.

[14] M. Esmaily, N. Mortazavi, J.E. Svensson, M. Halvarsson, A.E.W. Jarfors, M. Wessén, R. Arrabal, L.G. Johansson, On the microstructure and corrosion behavior of AZ91/SiC composites produced by rheocasting, Mater. Chem. Phys. 180 (2016) 29–37, https://doi.org/10.1016/j.matchemphys.2016.05.016.

[15] G. Yuanding, Huang Sihang You, Karl Ulrich, Kainer Norbert, Hort Jian, Grain refinements of magnesium alloys inoculated by additions of external SiC particles, IOP Conf. Ser. Mater. Sci. Eng. (2019).

[16] Y. Huang, X. Zheng, A. Okechukwu, G.S. Kim, K.U. Kainer, N. Hort, Aluminium-rich coring structures in Mg-Al alloys with carbon inoculation, Mater. Sci. Forum 654–656 (2010) 675–678, https://doi.org/10.4028/www.scientific.net/MSF.654-656.675.

[17] Y. Huang, K.U. Kainer, N. Hort, Mechanism of grain refinement of Mg-Al alloys by SiC inoculation, Scr. Mater. 64 (2011) 793–796, https://doi.org/10.1016/j.scriptamat.2011.01.005.

[18] C.J. Lin, D. Wang, L. Peng, A. Zois, C.M. McGilvery, Q. Li, C.M. Gourlay, Carbides in AZ91 and their role in the grain refinement of magnesium, J. Alloy. Compd. 971 (2024), https://doi.org/10.1016/j.jallcom.2023.172655.

[19] L. Peng, G. Zeng, C.J. Lin, C.M. Gourlay, Al2MgC2 and AlFe3C formation in AZ91 Mg alloy melted in Fe-C crucibles, J. Alloy. Compd. 854 (2021) 156415, https://doi.org/10.1016/j.jallcom.2020.156415.

[20] Y. Xue, H. Li, L. Qi, L. Yang, J. Wang, Y. Ma, Interfacial microstructure and strengthening mechanisms of Cf/Mg composite with double-layer interface, Ceram. Int. 47 (2021) 31149–31159, https://doi.org/10.1016/j.ceramint.2021.07.289.

[21] J. Li, M. Zhang, J. Zhao, Y. Cui, X. Luo, Atomic insight into the interfacial bonding and role of carbon atoms on β-SiC(1 1 1)/Al2MgC2(0 0 0 1): a first-principles study, Appl. Surf. Sci. 511 (2020), https://doi.org/10.1016/j.apsusc.2020.145633.

[22] B. Watts, S. Finizio, K. Witte, M. Langer, S. Mayr, S. Wintz, B. Sarafimov, J. Raabe, Status of the PolLux STXM Beamline, Microsc. Microanal. 24 (2018) 476–477, https://doi.org/10.1017/S1431927618014617.

[23] K. Witte, A. Späth, S. Finizio, C. Donnelly, B. Watts, B. Sarafimov, M. Odstrcil, M. Guizar-Sicairos, M. Holler, R.H. Fink, J. Raabe, From 2D STXM to 3D imaging: soft X-ray laminography of thin specimens, Nano Lett. 20 (2020) 1305–1314, https://doi.org/10.1021/acs.nanolett.9b04782.

[24] S. Yoshioka, K. Tsuruta, T. Yamamoto, K. Yasuda, S. Matsumura, N. Ishikawa, E. Kobayashi, X-ray absorption near edge structure and first-principles spectral investigations of cationic disorder in MgAl2O4 induced by swift heavy ions, Phys. Chem. Chem. Phys. 20 (2018) 4962–4969, https://doi.org/10.1039/C7CP07591J.

[25] U. Flechsig, C. Quitmann, J. Raabe, M. Böge, R. Fink, H. Ade, The polLux microspectroscopy beam line at the swiss light source, AIP Conf. Proc. 879 (2007) 505–508, https://doi.org/10.1063/1.2436109.

[26] J. Raabe, G. Tzvetkov, U. Flechsig, M. Böge, A. Jaggi, B. Sarafimov, M.G. C. Vernooij, T. Huthwelker, H. Ade, D. Kilcoyne, T. Tyliszczak, R.H. Fink, C. Quitmann, PolLux: a new facility for soft x-ray spectromicroscopy at the swiss light source, Rev. Sci. Instrum. 79 (2008) 1–10, https://doi.org/10.1063/1.3021472.

[27] K. Pandey, K. Paredis, T. Hantschel, C. Drijbooms, W. Vandervorst, The impact of focused ion beam induced damage on scanning spreading resistance microscopy measurements, Sci. Rep. 10 (2020) 1–15, https://doi.org/10.1038/s41598-020-71826-w.

[28] B. Mingler, H.P. Karnthaler, Tem Studies of the Early Stages of Precipitation in Al-Mg-Si Alloys in Comparison with Electron Radiation Damage Effects, in: D. L. Dorset, S. Hovmöller, X. Zou (Eds.), BT - Electron Crystallography, Springer Netherlands, Dordrecht, 1997, pp. 397–400, https://doi.org/10.1007/978-94-015-8971-0_40.

[29] A.P. Hitchcock, Analysis of X-ray images and spectra (aXis2000): a toolkit for the analysis of X-ray spectromicroscopy data, J. Electron Spectros. Relat. Phenom. 266 (2023) 147360, https://doi.org/10.1016/j.elspec.2023.147360.

[30] W. Klysubun, P. Kidkhunthod, P. Tarawarakarn, P. Sombunchoo, C. Kongmark, S. Limpijumnong, S. Rujirawat, R. Yimnirun, G. Tumcharern, K. Faungnawakij, SUT-NANOTEC-SLRI beamline for X-ray absorption spectroscopy, J. Synchrotron Radiat. 24 (2017) 707–716, https://doi.org/10.1107/S1600577517004830.

[31] D. Li, M. Peng, T. Murata, Coordination and local structure of magnesium in silicate minerals and glasses: Mg K-edge XANES study, Can. Mineral. 37 (1999) 199–206.

[32] T.S. Arthur, P.A. Glans, M. Matsui, R. Zhang, B. Ma, J. Guo, Mg deposition observed by in situ electrochemical Mg K-edge X-ray absorption spectroscopy, Electrochem. Commun. 24 (2012) 43–46, https://doi.org/10.1016/J.ELECOM.2012.08.018.

[33] M. Newville, Larch: an analysis package for XAFS and related spectroscopies, J. Phys. Conf. Ser. 430 (2013), https://doi.org/10.1088/1742-6596/430/1/012007.

[34] G. Deffrennes, B. Gardiola, E. Jeanneau, G. Mikaelian, P. Benigni, A. Pasturel, A. Pisch, J. Andrieux, O. Dezellus, Synthesis, crystallographic structure and thermodynamic properties of T2-Al 2 MgC 2, J. Solid State Chem. 273 (2019) 150–157, https://doi.org/10.1016/j.jssc.2019.02.039.

[35] F. Bosselet, B.F. Mentzen, J.C. Viala, M.A. Etoh, J. Bouix, Synthesis and structure of T2-Al2MgC2, Eur. J. Solid State Inorg. Chem. 35 (1998) 91–99, https://doi.org/10.1016/S0992-4361(98)80017-9.

[36] E. Piskorska, K. Lawniczak-Jablonska, R. Minikayev, A. Wolska, W. Paszkowicz, P. Klimczyk, E. Benko, Quantitative phase analysis of cubic boron nitride based composites by X-ray absorption near edge structure, Spectrochim. Acta - Part B At. Spectrosc. 62 (2007) 461–469, https://doi.org/10.1016/j.sab.2007.04.003.

[37] X. Hao, Z. Xu, G.M. Christopher, L. Qianqian, Grain refinement of magnesium castings using recycled machining chips, Unpubl. Results. (2024).

[38] T.J. Richardson, B. Farangis, J.L. Slack, P. Nachimuthu, R. Perera, N. Tamura, M. Rubin, X-ray absorption spectroscopy of transition metal-magnesium hydride thin films, J. Alloy. Compd. 356–357 (2003) 204–207, https://doi.org/10.1016/S0925-8388(02)01237-9.

[39] L. Peng, G. Zeng, D. Wang, J. Xian, S. Ji, H. Zhan, C.M. Gourlay, Al-Mn Intermetallics in High Pressure Die Cast AZ91 and Direct Chill Cast AZ80, (2022) 1–18.